



1 **Prediction of basin-scale river channel migration based on**
2 **landscape evolution numerical simulation**

3

4 Jitian Wu¹, Xiankui Zeng¹, Qihui Wu¹, Dong Wang¹, and Jichun Wu¹

5 ¹ Key Laboratory of Surficial Geochemistry, Ministry of Education, School of Earth

6 Sciences and Engineering, Nanjing University, Nanjing 210023, China

7 **Correspondence:** Xiankui Zeng (xiankuizeng@nju.edu.cn)

8 Submitted to *Hydrology and Earth System Sciences*

9



10 **Abstract**

11 The basin-scale river channel migration, driven by multiple factors such as
12 hydrometeorological conditions, tectonic movements, and human activities, exerts a
13 profound influence on regional morphological features, water resource, and ecosystem
14 over long-term evolution. Conventional river dynamics approaches struggle to
15 quantitatively characterize basin-scale channel migration due to difficulties in
16 incorporating factors like basin hydrological processes and tectonic activities. This study
17 proposed a novel technique for the numerical simulation of river channel migration,
18 integrating a fully coupled multi-processes landscape evolution model (e.g., hydrological,
19 geomorphic and tectonic processes) with channel extraction. Furthermore, to address
20 model parameter uncertainty, a Markov chain Monte Carlo (MCMC) method with
21 a modified likelihood function is used for parameter uncertainty quantification.
22 Simultaneously, a computationally efficient Long Short-Term Memory (LSTM)-based
23 surrogate model for channel migration is developed to overcome the computational
24 bottleneck in uncertainty analysis. Applied to the Kumalake River Basin within China's
25 Tarim Basin, the study employs the Landscape Evolution-Penn State Integrated
26 Hydrologic Model (LE-PIHM) to construct the landscape evolution model. Combined with
27 channel extraction, it simulates historical (2000-2021) and future (2021-2100) landscape
28 evolution and channel migration processes. Results demonstrated that the developed river
29 channel migration model, aided by parameter uncertainty analysis, reliably captures the
30 dynamics of channel migration in the study area during 2000-2021. Additionally, the
31 LSTM-based surrogate model achieves high accuracy, effectively resolving computational
32 challenges in parameter uncertainty analysis. Predictions under different climate scenarios



33 reveal significant variations in future channel evolution, indicating that climate change will
34 profoundly reshape basin geomorphic features and river patterns.
35



36 **1. Introduction**

37 Basin-scale river channel migration is the result of interactions among multiple
38 spheres within the complex earth system, influenced by various factors including
39 meteorological, hydrological, and geological conditions (Li et al., 2023; Desormeaux et al.,
40 2021). Over long temporal and basin scales, river channel migration regulates the spatial
41 configuration of river networks, exerting significant impacts on regional water resources,
42 ecological environments, and the development of civilizations. For instance, the substantial
43 downstream migration of the Euphrates River between approximately 2112–2004 BCE
44 contributed to the collapse of the Sumerian civilization (Hritz et al., 2010). The diversion
45 of the lower Tarim River in 630 CE led to the disappearance of the ancient Loulan Kingdom
46 (Yu et al., 2016; Shao et al., 2022). Quantitative research on river channel migration at the
47 basin scale is crucial; it can not only inform projections of water resource distribution under
48 climate change scenarios but also facilitate the reconstruction of linkages among channel
49 evolution, fluvial ecosystems, and the trajectories of human civilizations (Hickin 1983;
50 Zhou et al., 2022; Zhen et al., 2025).

51 River channel migration in the basin scale involves multiple coupled processes
52 including surface water and groundwater flow, weathering and erosion, and tectonic uplift.
53 These processes operate across broad spatiotemporal scales, exhibit complex mechanistic
54 interactions, and are highly susceptible to anthropogenic disturbance. Numerical modeling
55 serves as the principal approach for quantitatively characterizing these dynamics. Among
56 various modeling strategies, river channel migration models grounded in fluvial dynamics
57 have been widely used. For example, Ikeda et al. (1981) developed a single meander
58 segment model by coupling flow fields with erosion rates. Morón et al. (2017) employed



59 Delft3D (Lesser et al., 2004) to simulate the evolution of channel segments in the Nile
60 River, Columbia River, Congo River and Negro River. Hsu et al. (2022) utilized Nays2DH
61 (Ali et al., 2017) to simulate braided river morphology in the lower Dajia River, and
62 identified that channel width as a primary factor governing migration direction. However,
63 these methods generally focus on partial river channel domains (e.g., meander reaches) and
64 fail to incorporate hydrologic processes and tectonic activities at the basin scale, thus
65 limiting their applicability to river channel migration over engineering timescales and
66 channel segment scales.

67 As a typical geomorphic unit, river channels are fundamentally governed by landscape
68 evolution processes (Lisenby et al., 2020). Landscape evolution models (LEMs) are
69 numerical tools designed to quantify elevation changes across watersheds over geological
70 timescales, incorporating hydrologic processes and tectonic uplift (Bishop, 2007; Tucker
71 and Hancock, 2010; Hou et al., 2025). By integrating LEMs with river channel extraction
72 techniques, it becomes feasible to simulate long-term, basin-scale channel migration.
73 Commonly used LEMs include CASCADE (Braun et al., 1997), CHILD (Tucker et al.,
74 2001), CAESAR-Lisflood (Coulthard et al., 2013), DAC (Goren et al., 2014; Yang et al.,
75 2015), Landlab (Barnhart et al., 2020; Litwin et al., 2024), all of which have been widely
76 used for simulating landscape evolution. Nevertheless, these models often simplify or
77 neglect groundwater dynamics and lateral erosion processes (Whipple et al., 2017), making
78 it difficult to accurately capture these crucial hydrological and geomorphic processes in
79 large-scale, long-term watershed landscape evolution simulations.

80 Zhang et al. (2016) developed LE-PIHM by coupling surface-subsurface hydrologic
81 processes with slope and channel sediment transport, while accounting for bedrock



82 weathering and tectonic uplift, based on the PIHM framework (Qu et al., 2007). LE-PIHM
83 is particularly suited for quantifying landscape evolution processes over long durations and
84 basin extents.

85 Nevertheless, current studies rarely integrate multiple processes for real basin-scale
86 simulations of coupled landscape evolution and river channel migration. Meanwhile,
87 LEMs contain a large number of parameters to be identified, the non-negligible parameters
88 uncertainty can lead to unreliable simulations of landscape evolution and river channel
89 migration, which has not been adequately addressed in current researches (Temme et al.,
90 2009; Neuendorf et al., 2018). To quantify river channel migration at the basin scale under
91 the coupled effects of multiple processes, the LE-PIHM was used to establish a landscape
92 evolution model in this study, and the distribution of river channels was identified using a
93 river channel extraction technique. In addition, Long Short-Term Memory (LSTM)
94 surrogate modeling and Bayesian uncertainty analysis were employed to quantify
95 parameter uncertainty in the LEM.

96 This study selects the Kumalake River Basin within China's Xinjiang Tarim Basin as
97 the research area. This basin features diverse geomorphic types and complex climatic
98 conditions, and has experienced significant river channel migration in recent decades
99 (Wang et al., 2024), making it an ideal site for conducting basin-scale simulations of terrain
100 evolution and river channel dynamics. Based on the identified model parameters
101 distribution of LE-PIHM, the river channel migration process in the study area over the
102 past two decades was quantitatively reconstructed. Finally, this study conducted future
103 scenario simulations of landscape evolution and river channel migration under projected
104 climate change through the end of the 21st century.



105 The structure of this paper is as follows: Sect. 2 outlines the methodology and overall
106 workflow; Sect. 3 introduces the construction of the basin-scale river channel migration
107 model and the development of an LSTM-based surrogate model for uncertainty analysis;
108 Sect. 4 presents the results and discussion; and Sect. 5 provides concluding remarks and
109 summarizes the key findings.

110 **2. Methodology**

111 **2.1 Framework of basin-scale river channel migration prediction**

112 The framework of predicting basin-scale river channel migration in this paper consists
113 of three parts (Fig. 1).

114 Part 1: Establishment of the basin-scale river channel migration model. The basin-
115 scale river channel migration model is implemented in two steps. First, landscape evolution
116 is simulated using LE-PIHM to obtain the elevation distribution of the study area.
117 Subsequently, the DEM is processed using the D8 algorithm to extract the spatial
118 distribution of river channel.

119 Part 2: Development of a LSTM-based surrogate model for efficient parameter
120 uncertainty analysis. To improve the efficiency of parameter identification, a surrogate
121 model corresponding to the original river channel migration model (Part 1) is developed
122 for the reconstruction period (2000–2021). Parameter sensitivity analysis is first conducted
123 to identify the key landscape evolution parameters of LE-PIHM. Then, 3,000 parameter
124 sets are sampled and input into the basin-scale river channel migration model (Part 1) to
125 generate the associated planar channel coordinates, which serve as the training datasets.
126 The LSTM is trained using these data to construct a surrogate model of basin-scale river
127 channel migration, substantially reducing the computational burden of parameter



128 uncertainty analysis.

129 Part 3: Parameter uncertainty analysis and the prediction of channel migration. Based
130 on the LSTM-based surrogate model (Part 2), parameter uncertainty analysis is conducted
131 using a modified-likelihood Markov chain Monte Carlo (MCMC) approach constrained by
132 observed river channel data from 2000 to 2021. The resulting posterior distribution of river
133 channel enable the reconstruction of channel migration processes over 2000–2021. The
134 maximum-likelihood posterior parameter set is then selected, and the original river channel
135 migration model (Part 1) is executed under future climate scenarios to predict channel
136 migration from 2021 to 2100.

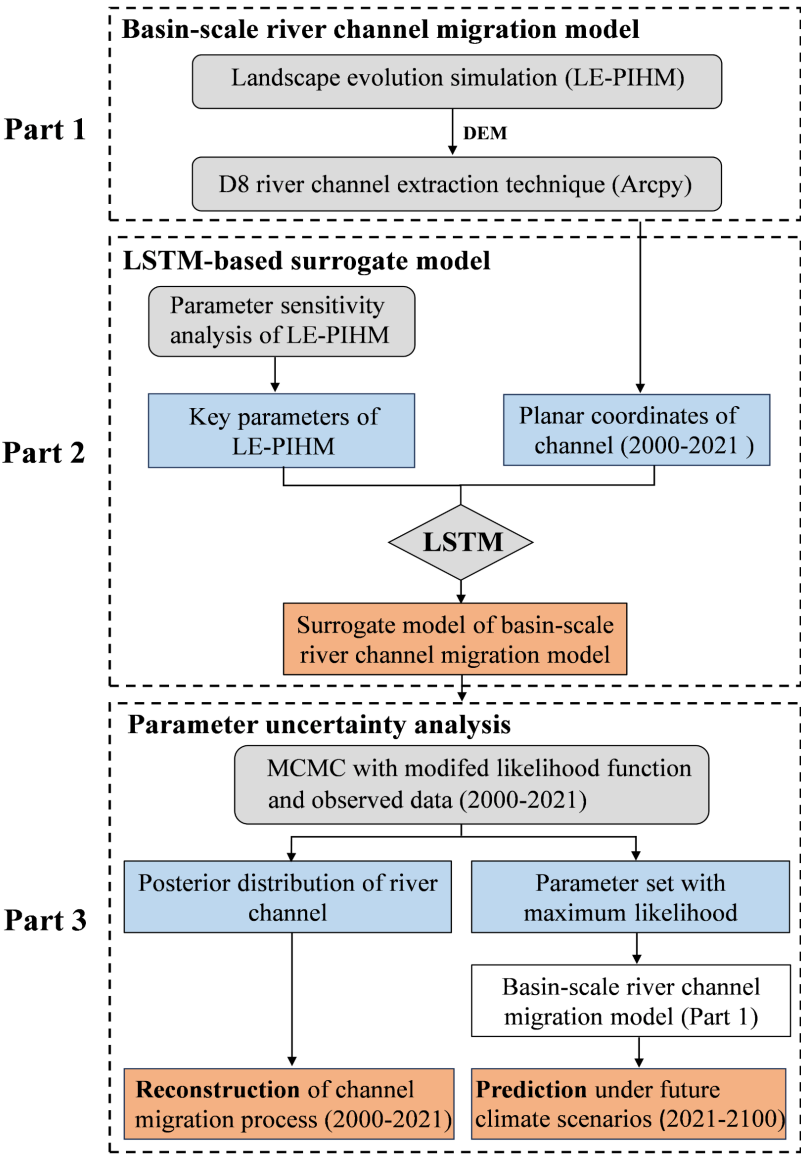


Figure 1. Technical roadmap of basin-scale river channel migration prediction

2.2 Basin-scale river channel migration model

2.2.1 Landscape evolution simulation

The Landscape Evolution–Penn State Integrated Hydrologic Model (LE-PIHM) was used to simulate the landscape evolution processes. LE-PIHM couples the processes of



143 surface water and groundwater, snow accumulation and melt, hillslope and river channel
 144 sediment transport, weathering and erosion, as well as tectonic uplift (Fig. 2). It is a basin-
 145 scale fully coupled hydrologic-process-based landscape evolution model (Zhang et al.,
 146 2016).

147 The model simulates surface elevation change based on the principle of mass
 148 continuity. According to the law of mass conservation, the geomorphic process equation
 149 can be expressed as the temporal variation of the mass of the regolith and bedrock.

$$\begin{aligned}
 \frac{\partial(\sigma_{re} h dx dy)}{\partial t} + \frac{\partial(\sigma_{ro} e dx dy)}{\partial t} = & \sigma_{re} q_c dy - [\sigma_{re} q_c dy + \frac{\partial(\sigma_{re} q_c dy)}{\partial x} dx] \\
 & + \sigma_{re} q_c dx - [\sigma_{re} q_c dx + \frac{\partial(\sigma_{re} q_c dy)}{\partial y} dy] \\
 & + \sigma_{re} q_s dy - [\sigma_{re} q_s dx + \frac{\partial(\sigma_{re} q_s dy)}{\partial x} dx] \\
 & + \sigma_{re} q_s dx - [\sigma_{re} q_s dx + \frac{\partial(\sigma_{re} q_s dy)}{\partial y} dy] \\
 & + \sigma_{ro} U dx dy
 \end{aligned} \tag{1}$$

151 where σ_{re} is the bulk density of regolith (kg/m^3); σ_{ro} is the bulk density of bedrock (kg/m^3);
 152 h is the regolith thickness (m); e is the elevation of the bedrock surface (m); The regolith
 153 thickness h is defined as the difference between the ground surface elevation z and the
 154 bedrock elevation e ; q_c is the lateral volumetric flux of regolith (m^2/yr), driven by processes
 155 such as soil creep; q_s is the surface sediment flux by overland flow (m^2/yr); U is the tectonic
 156 uplift rate (m/yr).

157 The governing equations for hydrologic processes describe the water flux dynamics
 158 from the vegetation canopy to the regolith layer. These processes can be represented as
 159 follows:



$$\begin{cases}
 \frac{\partial \psi_{\text{canopy}}}{\partial t} = vFrac(1 - f_s)p - E_c - TF \\
 \frac{\partial \psi_{\text{snow}}}{\partial t} = f_s p - SM \\
 \frac{\partial \psi_{\text{surf}}}{\partial t} = \nabla q_{\text{sw}} + p_{\text{net}} - I - E_s \\
 \frac{\partial \psi_{\text{unsat}}}{\partial t} = I - R - E_g - E_{\text{gt}} \\
 \frac{\partial \psi_{\text{sat}}}{\partial t} = \nabla q_{\text{gw}} + R - E_{\text{sat}} - E_{\text{tsat}}
 \end{cases} \quad (2)$$

161 where: ψ_{canopy} is the canopy water storage (m); ψ_{snow} is the snow depth (m); ψ_{surf} is the
 162 surface water depth (m); ψ_{unsat} is the water storage in the unsaturated zone (m); ψ_{sat} is
 163 the groundwater (saturated zone) storage (m); $vFrac$ is the fraction of vegetation
 164 coverage; f_s is the fraction of precipitation falling as snow; P is the precipitation rate
 165 (m/day); E_c and E_s are the evaporation rates from the canopy and surface water, respectively
 166 (m/day); TF is the throughfall rate from canopy to ground (m/day); SM is the snowmelt rate
 167 (m/day); p_{net} is the net precipitation reaching the ground surface (m/day); I is the
 168 infiltration rate (m/day); E_g and E_{sat} are the evaporation rates from the unsaturated and
 169 saturated zones, respectively (m/day); E_{gt} and E_{tsat} are the transpiration rates from the
 170 unsaturated and saturated zones, respectively (m/day); q_{sw} is the unit-width overland flow
 171 rate (m²/day); q_{gw} is the unit-width groundwater (lateral) flow rate (m²/day).

172 The values of q_{sw} and q_{gw} are determined by the Manning equation and Darcy's law,
 173 respectively, as follows:

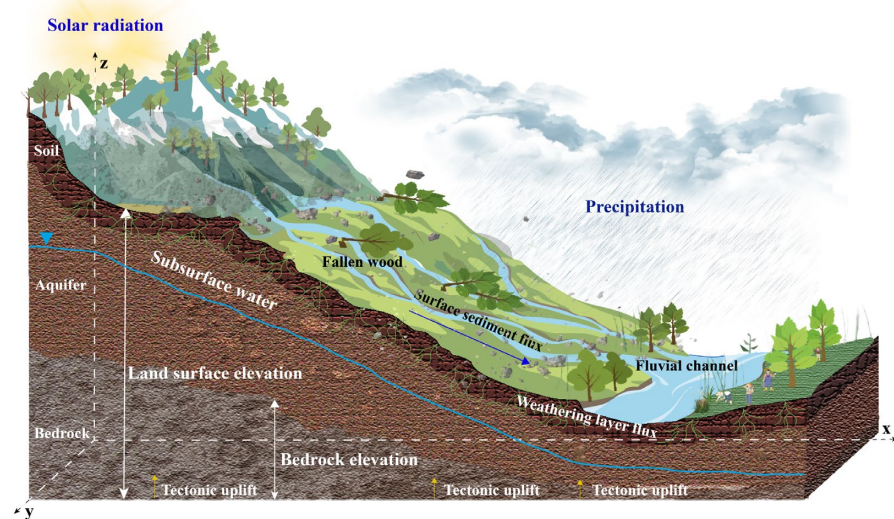
$$q_{\text{sw}} = \frac{\psi_{\text{surf}}^{5/3}}{n_s} (\nabla(\psi_{\text{surf}} + z))^{1/2} \quad (3)$$

$$q_{\text{gw}} = \psi_{\text{sat}} k_{\text{sat}} \nabla(\psi_{\text{sat}} + e) \quad (4)$$



176 where n_s is the Manning's roughness coefficient; k_{sat} is the horizontal hydraulic
 177 conductivity of the aquifer (m/day). For detailed formulas and variable descriptions, please
 178 refer to Qu and Duffy (2007).

179 The above governing equations (1-4) couple hydrological processes, hillslope and
 180 channel sediment transport processes, and tectonic movements to form a state-of-the-art
 181 hydro-geomorphic model for simulating landscape evolution.



182
 183 **Figure 2.** Schematic diagram of the Landscape evolution process.

184 2.2.2 D8 algorithm river channel extraction technique

185 The river channel extraction in basin-scale is implemented through a topography-
 186 based extraction technique. This technique is based on the principle of maximum gradient
 187 and identifies river channels within the watershed using surface elevation data. Specifically,
 188 the landscape evolution simulation provides the surface elevation distribution of the study
 189 area, from which a digital elevation model (DEM) is constructed. The DEM is first filled
 190 to remove depressions, followed by spatial analysis to determine surface flow direction and



191 compute flow accumulation. River channel distribution is then extracted based on the
192 accumulated flow.

193 The standard D8 algorithm, known for its simplicity and practicality, is currently the
194 most widely used and reliable method for determining water flowpaths from DEM
195 (O'Callaghan & Mark, 1984; Tarboton, 1997). The ArcPy scripting in ArcGIS, which
196 implements the standard D8 algorithm (Esri, 2022), will be used in this study to extract
197 watershed river channels through the ArcGIS hydrological analysis platform.

198 **2.2.3 Long Short-Term Memory algorithm**

199 Long Short-Term Memory (LSTM) is a specialized type of Recurrent Neural Network
200 (RNN), originally proposed by Hochreiter et al. (1997) and later extended and popularized
201 by Graves et al. (2005). Traditional RNNs often suffer from the vanishing or exploding
202 gradient problem when processing long sequential data, making it difficult to capture long-
203 term dependencies effectively. LSTM addresses this issue by introducing gated
204 mechanisms namely the forget gate, input gate, and output gate, which dynamically
205 regulate the flow of information. These gates allow the network to selectively store, update,
206 and output information within memory cells, thereby effectively addressing the gradient
207 instability problem in long-sequence modeling.

208 To address the computational burden caused by repeated model evaluations during
209 the parameter uncertainty analysis of the basin-scale river channel migration model, this
210 study constructs a surrogate model using an LSTM network. Specifically, the LSTM
211 algorithm is employed to build the nonlinear response relationship between the key
212 parameters of LE-PIHM and the spatial distribution of river channels (i.e., planar
213 coordinates of reaches) within the study area.



214 **2.3 Bayesian uncertainty analysis**

215 **2.3.1 Markov chain Monte Carlo simulation**

216 Markov chain Monte Carlo (MCMC) is a statistical simulation technique based on
 217 Bayesian theory. Its core idea is to construct a Markov chain that iteratively explores the
 218 parameter probability space to generate samples from the target posterior distribution. As
 219 the chain evolves, its stationary distribution converges to the posterior distribution of the
 220 parameters of interest (Vrugt et al., 2009).

221 MCMC integrates observational data through Bayes' theorem, enabling parameter
 222 samples to progressively converge from the prior distribution $p(\theta)$ to the posterior
 223 distribution $p(\theta | D)$.

$$224 \quad p(\theta | D) = \frac{L(\theta | D)p(\theta)}{\int L(\theta | D)p(\theta)d(\theta)} \quad (5)$$

225 where $L(\theta | D)$ represents the likelihood function of a parameter sample θ , D represents
 226 the observed data. The likelihood function L is typically defined as a Gaussian likelihood
 227 function:

$$228 \quad L(\theta^i | D) = \frac{1}{2\pi^{n/2} |\Sigma|^{1/2}} \exp \left[-\frac{[D - f(\theta^i)]^T \Sigma^{-1} [D - f(\theta^i)]}{2} \right] \quad (6)$$

229 where n is the number of observed data points, $f(\theta^i)$ denotes the hydrologic model
 230 simulation result given the parameter θ^i , and Σ is the covariance matrix of the simulation
 231 residuals.

232 **2.3.2 Hausdorff distance and the modified likelihood function**

233 This study uses the average Hausdorff distance as a metric to quantify the discrepancy
 234 between the simulated river channel and the real river channel. The Hausdorff distance is
 235 an effective tool for assessing positional differences between two curves (Schütze et al.,



2012), and is suitable for quantitatively evaluating the spatial deviation associated with river channel migration.

The core concept of the Hausdorff distance is to treat two curves as two sets of discrete points. Suppose we have two point-sets, $A = \{a_1, \dots, a_p\}$, $B = \{b_1, \dots, b_q\}$, p and q represent the number of points in sets A and B , respectively, the bidirectional Hausdorff distance $HD(A, B)$ between sets A and B is defined as:

$$HD(A, B) = \text{Max} [h(A, B), h(B, A)] \quad (7)$$

where $h(A, B)$ and $h(B, A)$ represent the one-sided Hausdorff distances. Specifically, $h(A, B)$ denotes the set of minimum distances from each point in set A to the nearest point in set B , $h(A, B) = h(a_{1\min}, a_{2\min}, \dots, a_{p\min})$, where $a_{1\min}$ is the minimum distance from point a_1 to the points in set B . Similarly, $h(B, A)$ denotes the set of minimum distances from each point in B to the nearest point in A .

In this study, we modified Eq. (7) by replacing the maximum operation in the one-sided distance with the mean of the minimum distances, and set p equal to q . This modification better captures the overall spatial discrepancy between two river channel curves and is referred to as the average Hausdorff distance (H). A smaller value of H indicates that the simulated river channel more closely matches the observed channel.

$$H = \frac{1}{2p} \sum_{i=1}^p [h(A, B) + h(B, A)] \quad (8)$$

In the uncertainty analysis of river channel migration simulation, the likelihood function quantifies the degree of fit between the simulated and observed river channels. To enable the parameter uncertainty quantification through MCMC, the original likelihood function (i.e., Eq. (6)) is revised by treating the average Hausdorff distance (H) as the



simulation target. The observed value of H (denoted as H_{obs}) is set to 0, this indicates the H between the real river channel and itself. Thus, the residuals in the likelihood function can be expressed as:

$$H_{obs} - H = 0 - H = -H \quad (9)$$

combining Equation (6) with Equation (9) and taking the natural logarithm, a modified likelihood function designed for quantifying river channel simulation is obtained:

$$\ln L = -\frac{1}{2} \left[\frac{H^2}{\Sigma^2} + \ln(2\pi \Sigma^2) \right] \quad (10)$$

In other words, this modified form of the likelihood function (Equation 10) is used in the MCMC-based uncertainty analysis of river channel model parameters.

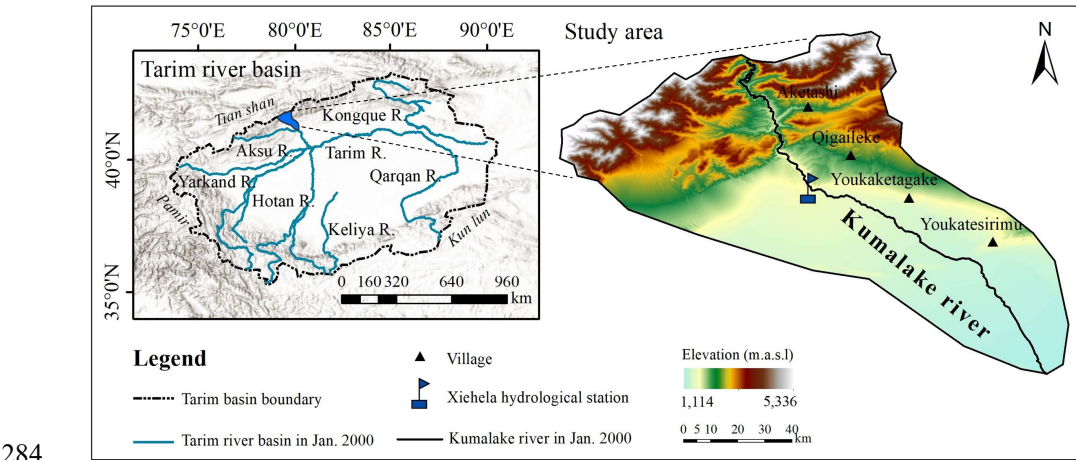
3. Construction of the river channel migration model

3.1 Study area

The Kumalake River Basin is located in the northwestern corner of the Tarim Basin in Xinjiang, China, covering an area of about 3,500 square kilometers. The basin is bordered by the towering Tianshan mountains to the north, the flat Aksu Plain to the south, and the Toxkan River Basin to the west. The landscape exhibits a distinct elevation gradient sloping from north to south, with a complex geomorphic setting comprising mountainous hillslopes, valley plains, and fluvial terraces (Fig. 3). The Kumalake River, approximately 89.34 km in length, is the largest tributary of the Aksu River. It flows from the northwest to the southeast across the study area and exits at the southeastern edge of the basin, where it joins the Tuoshigan River. The combined flow continues into the Aksu River and eventually discharges into the main stem of the Tarim River (Tang et al., 2007).



279 The Kumalake River has experienced pronounced channel migration during the last
280 two decades. This study selects the Kumalake River Basin as the case study area, with a
281 focus on simulating river channel migration over the period from 2000 to 2021. The
282 simulation is conducted within the landscape evolution modeling framework, and a
283 parameter uncertainty analysis is performed to improve the reliability of the model outputs.



284
285 **Figure 3.** Schematic diagram of the watershed in the study area. Basemap: Esri World
286 Hillshade (Esri).

287 3.2 Model input data

288 In this study, LE-PIHM combined with a river channel extraction technique is
289 employed to simulate the spatial distribution of river channels. Notably, four categories of
290 physical properties within the study area, i.e., soil, aquifer, bedrock, and land cover, exhibit
291 significant spatial heterogeneity (see Table 1 and Fig. 4). The driving force data in LE-
292 PIHM primarily include leaf area index, precipitation rate, air temperature, downward
293 shortwave radiation, snowmelt rate, wind speed, and relative humidity (Table 1)

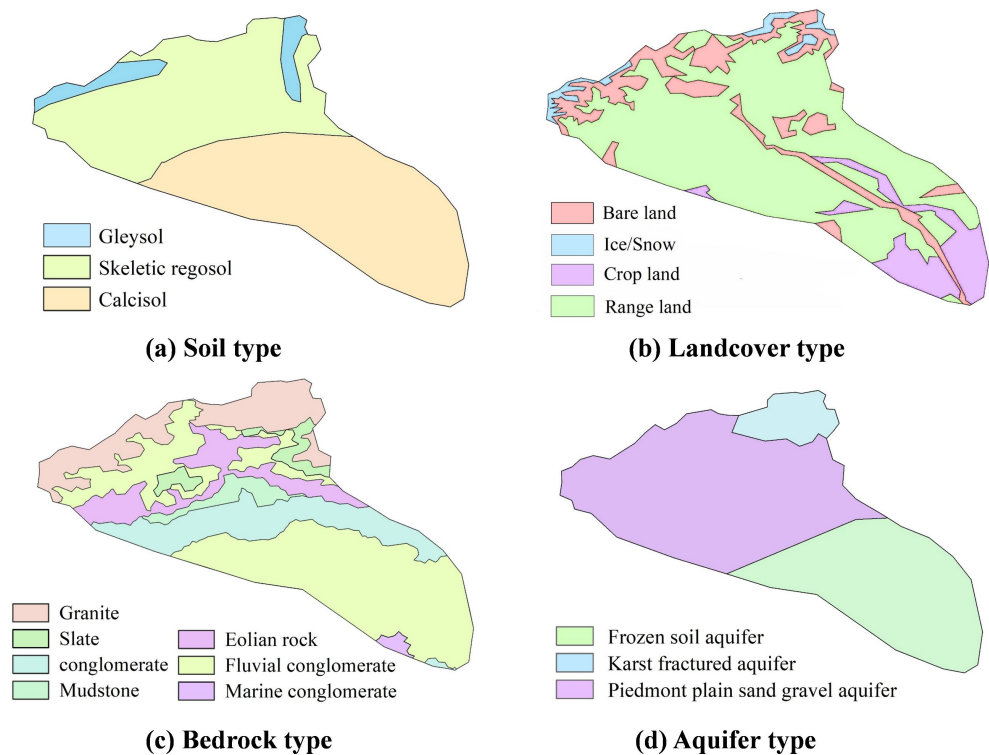
294 **Table 1.** Types and sources of input data for the landscape evolution model.

Data Type	Spatial Resolution	Temporal Resolution	Data Source	URL
Soil type	1:5000000	/	Food and Agriculture Organization of the UN	https://data.apps.fao.org/?lang=en
Bedrock type	1:1000000	/	International Soil Reference and Information Center	https://soilgrids.org/
Land cover	10 m	/	Environmental Systems Research Institute, Inc	https://livingatlas.arcgis.com/landcover/
Aquifer type	/	/	China Cartographic Publishing House	https://www.sinomaps.com/pub/
Leaf area index	0.5°×0.625°	1h	National Aeronautics and Space Administration	https://www.nasa.gov/
Surface roughness	0.5°×0.625°	1h		
Precipitation rate	0.25°	3h		
Air temperature	0.25°	3h		
Shortwave radiation	0.25°	3h		
Canopy interception storage	0.25°	3h		
Soil water storage	0.25°	3h		
Snow depth	0.25°	3h		
Snow melt rate	0.25°	3h		
Wind speed	0.25°	3h		
Relative humidity	1.25°	3h	International Soil Reference and Information Center	https://isric.org/
Initial surface elevation	30 m	/		
Initial bedrock depth	250 m	/		

All links in the table were last accessed on 2 December 2025

295

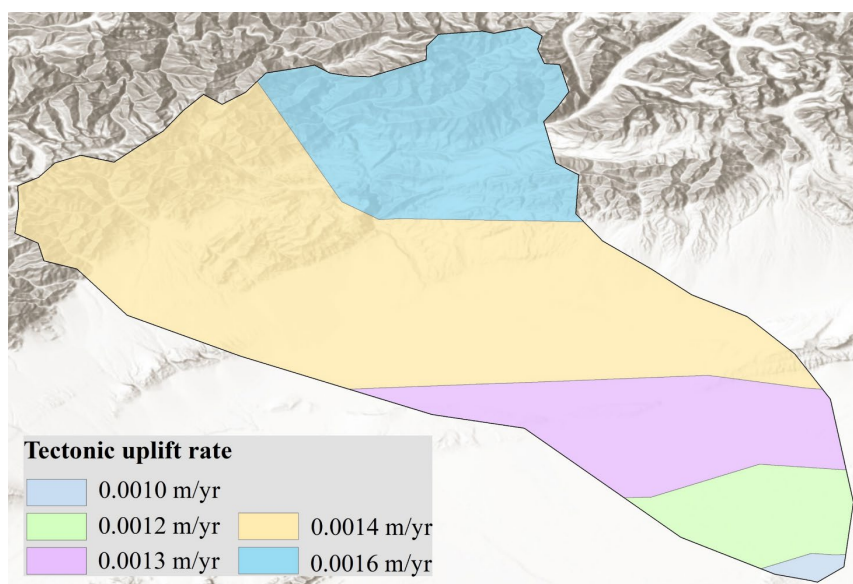




296

297 **Figure 4.** Zonation of average tectonic uplift rates in the study area from 2000 to 2021.

298 As an essential driving factor in landscape evolution, the rock uplift rate data were
299 derived from the vertical crustal velocity field of China (Wang et al., 2020; Zubovich et al.,
300 2016), with the Chinese GNSS velocity field taken from Wang and Shen (2020;
301 <https://doi.org/10.7910/DVN/C1WE3N>) and the Pamir–Tien Shan GNSS velocities from
302 Zubovich et al. (2016; <https://doi.org/10.1002/2015TC004055>). The spatial distribution of
303 the average rock uplift rate in the study area from 2000 to 2021 was obtained through
304 kriging interpolation (Fig. 5).



305

306 **Figure 5.** Zonation of average tectonic uplift rates in the study area from 2000 to 2021.

307 Basemap: Esri World Hillshade (Esri).

308 **3.3 Observed river channel planform data**

309 Observed river channel planform data for December 2007, February 2014, and
 310 December 2021 were obtained using the Google Earth Pro image platform (see Fig. 6).
 311 Among these, the spatial distribution of river channels from December 2007 and February
 312 2014 were used to identify the posterior distribution of model parameters (i.e., key
 313 parameters of LE-PIHM), while the December 2021 data were employed to validate the
 314 river channel migration results.

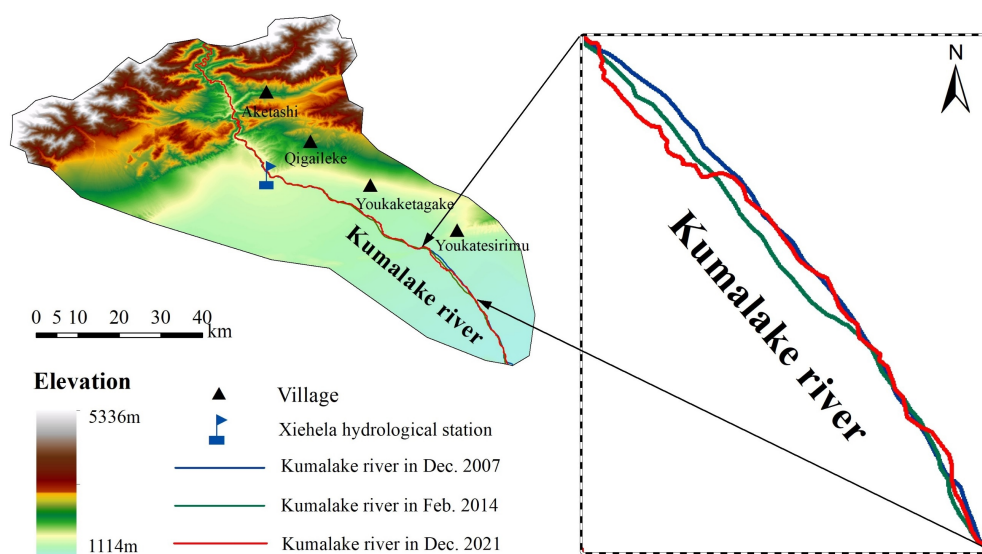


Figure 6. The spatial distribution of the Kumalake River channels in the study area.

3.4 Model settings

The outlet of the Kumalake River Basin was set at the intersection with the southeastern boundary of the study area, while all other boundaries were defined as no-flow boundaries. An unstructured triangular mesh was used to discretize the study area spatially. To accurately capture the landscape evolution processes in areas surrounding the river channel, mesh refinement was applied in the channel zones, with grid sizes less than 50 meters near the river. A total of 25,968 unstructured triangular elements were generated for the study area (see Fig. 7a).

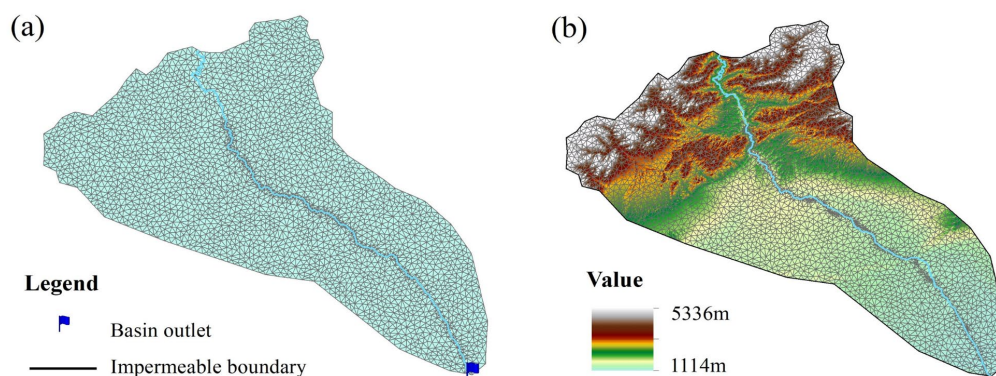


Figure 7. Mesh discretization and initial elevation grid of the research area.

The initial conditions required by LE-PIHM include ground surface elevation (Fig. 7b), canopy interception storage, snow depth, surface water depth, soil water storage, and groundwater storage. The canopy interception storage is initialized to 0 m in the model (Fig. 8 and Table 1).

The model was configured to run from January 2000 to December 2021, covering a total of 264 months (22 years). To capture the seasonal variability of hydrologic processes in the study area while controlling computational load, the time step was set to one month. The LE-PIHM model was executed on an Intel Xeon E5-2680 v3 server, with an average runtime per simulation of 195 minutes.

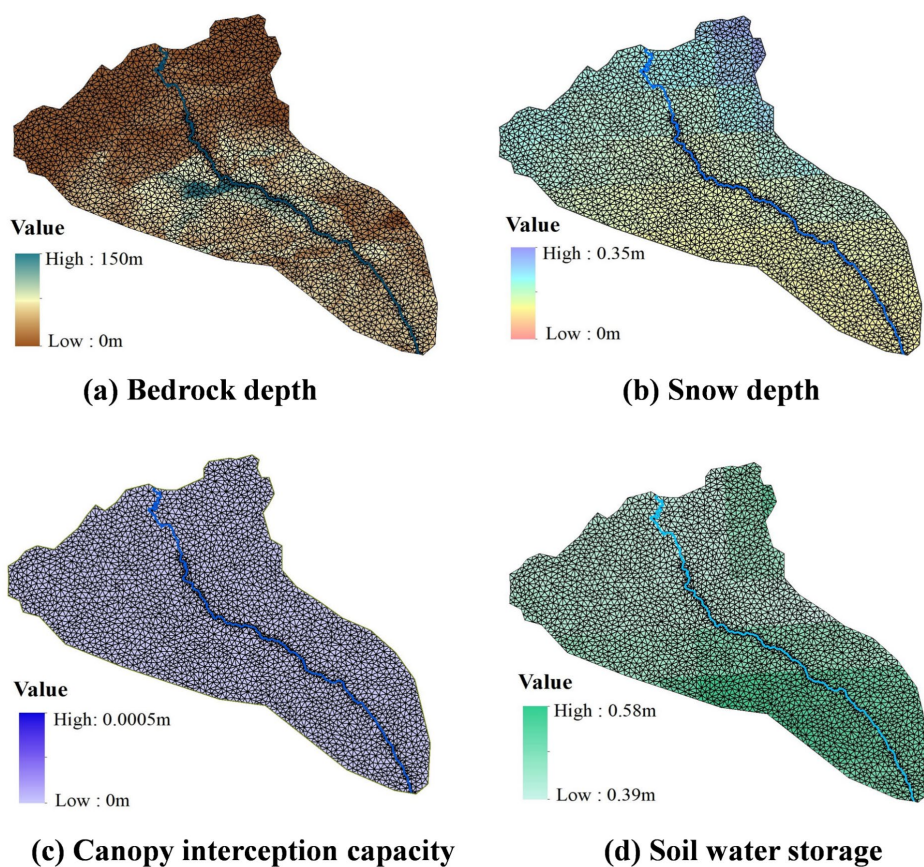


Figure 8. The initial conditions of landscape evolution model.

3.5 LSTM-based surrogate model for uncertainty analysis

After constructing the basin-scale channel migration model, the next part is to conduct parameter uncertainty analysis, followed by the reconstruction of river channel migration over 2000–2021 and the prediction of landscape evolution and river channel changes from 2021 to 2100 under future climate scenarios.

However, performing parameter uncertainty analysis using MCMC requires a large number of runs of the original model (i.e., the basin-scale channel migration model), which results in a significant computational burden. To reduce this computational cost, this study



346 employs an LSTM network to construct a surrogate model for river channel migration. The
 347 main steps and more details of LSTM-based surrogated models are as follows:

348 *i.* The Sobol method is applied for parameter sensitivity analysis. Considering the
 349 property parameters of surface cover, soil, aquifer, and bedrock, 11 highly sensitive
 350 parameters LE-PIHM are selected as the input variables for the surrogate model (Table 2).

351 **Table 2.** The parameters of landscape evolution model and their prior ranges.

Parameters	Units	Prior distribution
Vegetation fractional coverage (VegFrac)	/	[0.075, 0.225]
Root zone depth (Rzd)	m	[0.15, 0.45]
Soil vertical hydraulic conductivity (KV _s)	m/d	[0.30, 0.90]
Soil porosity (N _s)	/	[0.175, 0.525]
Morphological diffusivity (K ₁)	m ² /yr	[0.10, 0.30]
Soil particle diameter (D _s)	m	[0.0005, 0.0015]
Aquifer horizontal hydraulic conductivity (KH _g)	m/d	[3.50, 10.50]
Aquifer vertical hydraulic conductivity (KV _g)	m/d	[0.70, 2.10]
Bedrock weathering rate for bare rock (P ₀)	m/yr	[0.004, 0.012]
Tectonic uplift rate (U)	m/yr	[0.00050, 0.00155]
Coefficient for bedrock weathering equation (α)	1/m	[0.01, 0.03]

352 *ii.* Latin hypercube sampling is employed to generate 3,000 sample sets within the
 353 prior ranges of the input variables.

354 *iii.* These 3,000 parameter sets are individually input into the LE-PIHM model to
 355 generate surface elevation data at three time points, December 2007, February 2014, and
 356 December 2021. Subsequently, the corresponding spatial distribution of river channel is
 357 extracted through Arcpy scripting in ArcGIS. For each parameter set, the corresponding
 358 river channel is discretized uniformly into 2,000 points, producing 2,000 sets of planar
 359 coordinates of reaches.

360 *iv.* The obtained 3,000 sets of input variables and their corresponding coordinates are
 361 split into training and validation datasets at 70% and 30% ratios. The LSTM network is
 362 trained to learn the nonlinear mapping between the input variables and river channel



positions, thereby constructing a surrogate model for river channel migration. The network terminates in a fully connected output layer with a linear activation function and He-normal weight initialization. Training is performed using the Adam optimizer with a learning rate of 1×10^{-3} , minimizing the root-mean-square error (RMSE) between the predicted and reference river coordinate points. The model is trained for 10,000 epochs with a batch size of 100 and a validation split of 0.1.

As shown in the validation results (Table 3), the surrogate model constructed using LSTM demonstrates great predictive performance for river channel locations (i.e., the planar coordinates of river reaches). It achieved a mean absolute error (MAE) of 1,411.16 m, a root mean square error (RMSE) of 1,980.10 m, and a coefficient of determination (R^2) of 0.983. Furthermore, the average Hausdorff distance of the entire river between the surrogate model and original model outputs is 229.71 m. Given the total length of river channels in the study area is 89,337.95 m, this corresponds to only 0.25%. Thus, these results demonstrate that the surrogate model for basin-scale river channel migration exhibits high accuracy and reliability and can replace the original model for river channel dynamics simulation.

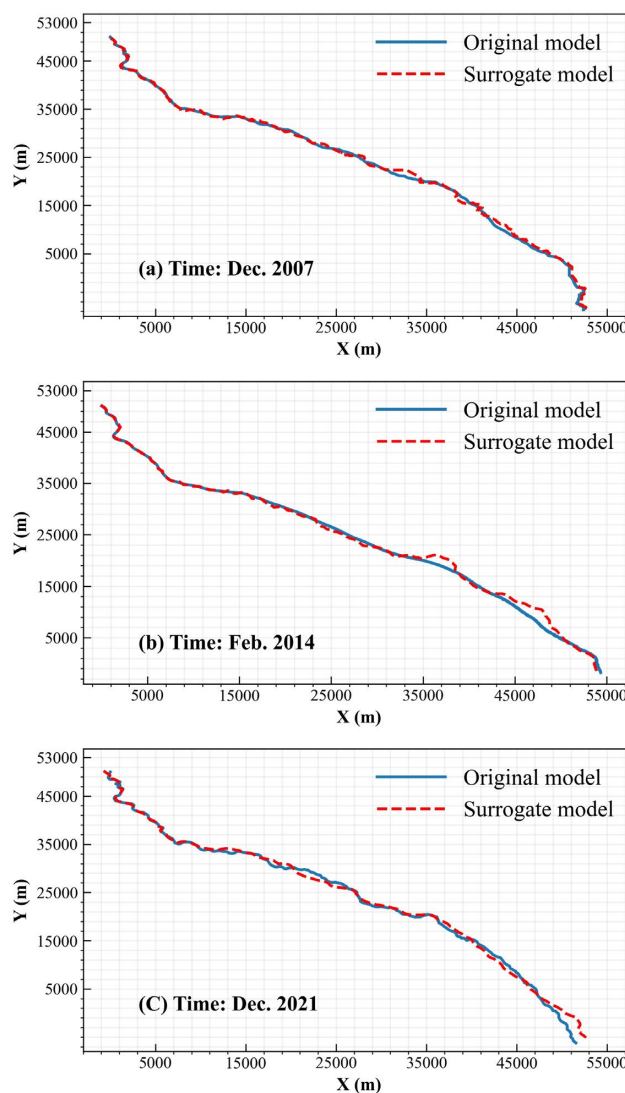
Table 3. Evaluations of the surrogate model for basin-scale river channel migration.

Metrics	RMSE	MSE	R^2	H/Total length of river
Results	1411.60m	1980.10m	0.98	0.0025

The spatial distribution of river channels predicted by the original model and the surrogate model are compared across three time points (Fig. 9). The surrogate model closely matches the original in the middle and upper reaches of the river channel, while some deviations occur in the downstream reaches. This discrepancy is primarily due to the mountainous topography upstream, where the landscape is rugged and river channels are



385 relatively stable. In contrast, the downstream region is a flat plain, where river channel
 386 migration is highly sensitive to model parameters, leading to slightly reduced accuracy in
 387 the surrogate model's performance in that area.



388
 389 **Figure 9.** Comparison between the original river channel migration model and the
 390 surrogate model at different time points.



391 Compared to the original model, the surrogate model for basin-scale river channel
392 migration achieves approximately a 20,000-fold increase in computational speed.
393 Therefore, employing this surrogate model in the parameter uncertainty analysis of river
394 channel migration can significantly reduce computational costs and effectively alleviate
395 the computational burden associated with the uncertainty analysis process.

396 **4. Results and discussion**

397 **4.1 Parameter uncertainty analysis**

398 **4.1.1 MCMC configuration**

399 The river channel migration model includes 11 unknown parameters to be identified,
400 with their prior distributions assumed to be uniform within the specified range (Table 2).
401 The MCMC simulation is performed using the DREAMzs sampling algorithm, with three
402 parallel Markov chains. Both the burn-in and formal sampling stages consist of 2,000
403 iterations. Additionally, the evolution of the Markov chains employs the modified
404 likelihood function described in Sect. 2.3.2. Based on the inferred posterior distributions
405 of the parameters, the posterior distribution of the river channel is obtained.

406 **4.1.2 Posterior distributions of model parameters**

407 The posterior probability density histograms of the river channel migration model
408 parameters through MCMC (Horizontal axis indicates the corresponding prior ranges; Fig.
409 10), together with the maximum likelihood parameter set (Table 4), show that the posterior
410 samples of the soil vertical hydraulic conductivity (KVs), aquifer vertical hydraulic
411 conductivity (KVg), soil particle diameter (Ds), bedrock weathering rate for bare rock (P0),
412 plant root depth (Rzd), vegetation fraction (VegFrac), and morphological diffusivity (K1)
413 converge to notably narrow intervals, indicating high sensitivity of these parameters to the



414 calibration data. In contrast, the fitting coefficient in the bedrock weathering equation (α)
 415 and the aquifer horizontal hydraulic conductivity (KHg) exhibit broader posterior
 416 distributions, although both display pronounced modes. Additionally, the posterior
 417 distributions of the bedrock uplift rate (U) and soil porosity (Ns) are relatively uniform and
 418 lack clear peak values, suggesting that considerable uncertainty remains for these
 419 parameters after identification.

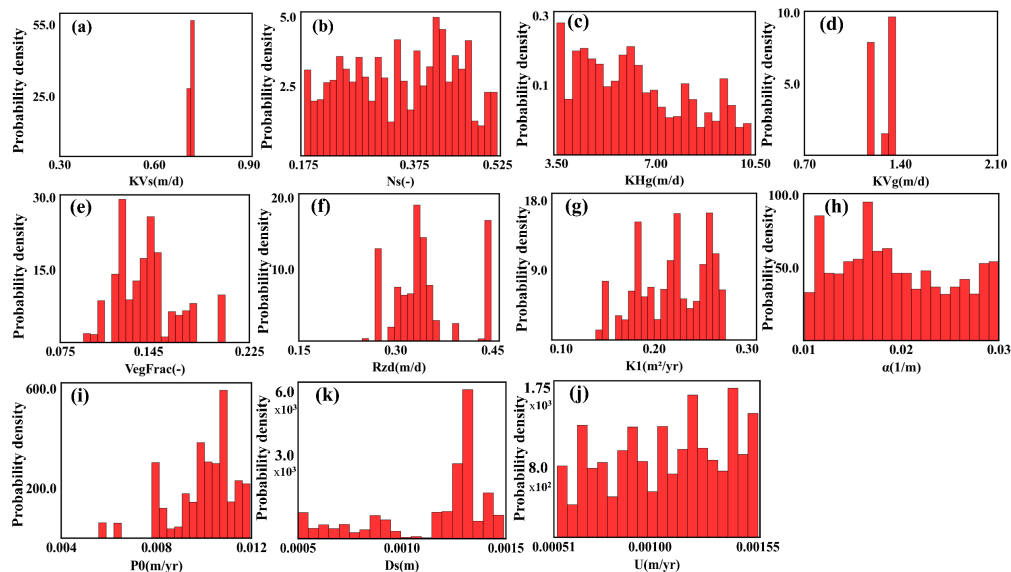


Figure 10. Calibrated posterior distributions of model parameters



Table 4. Parameter set corresponding to the maximum likelihood estimate.

Parameters	Units	Parameter value
Vegetation fractional coverage (VegFrac)	/	0.14
Root zone depth (Rzd)	m	0.17
Soil vertical hydraulic conductivity (KV _s)	m/d	0.43
Soil porosity (N _s)	/	0.24
Morphological diffusivity (K _l)	m ² /yr	0.20
Soil particle diameter (D _s)	m	0.001
Aquifer horizontal hydraulic conductivity (KH _g)	m/d	9.60
Aquifer vertical hydraulic conductivity (KV _g)	m/d	1.90
Bedrock weathering rate for bare rock (P ₀)	m/yr	0.007
Tectonic uplift rate (U)	m/yr	0.0008
Coefficient for bedrock weathering equation (α)	1/m	0.02

4.1.3 Reconstruction of river channel migration (2000-2021)

Based on the posterior distributions of the identified parameters, the river channel evolution from 2000 to 2021 in the study area was reconstructed. The result shows that the predicted confidence interval fully encompasses the observed river channel (Fig. 11), and the blue shaded region denotes the 95% confidence interval, the red line represents the observed river channel in Fig. 11. The average Hausdorff distance of the entire river between the simulated channel (marked in black line in Fig. 11) with the maximum likelihood parameter set and the observed channel is 225.42 m, which accounts for only 0.25% of the total river channel length. This indicates that the discrepancy between the simulated and observed river channel per unit length is minimal, demonstrating the high accuracy of the calibrated river channel migration model. Therefore, the river channel model facilitated by Bayesian parameter uncertainty quantification can reliably predict the river channel migration processes within the study area.

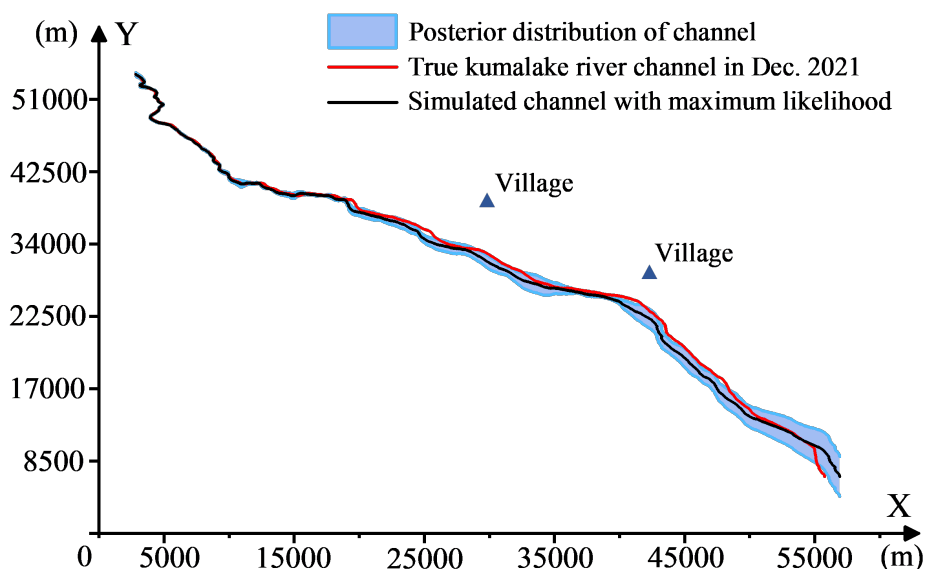
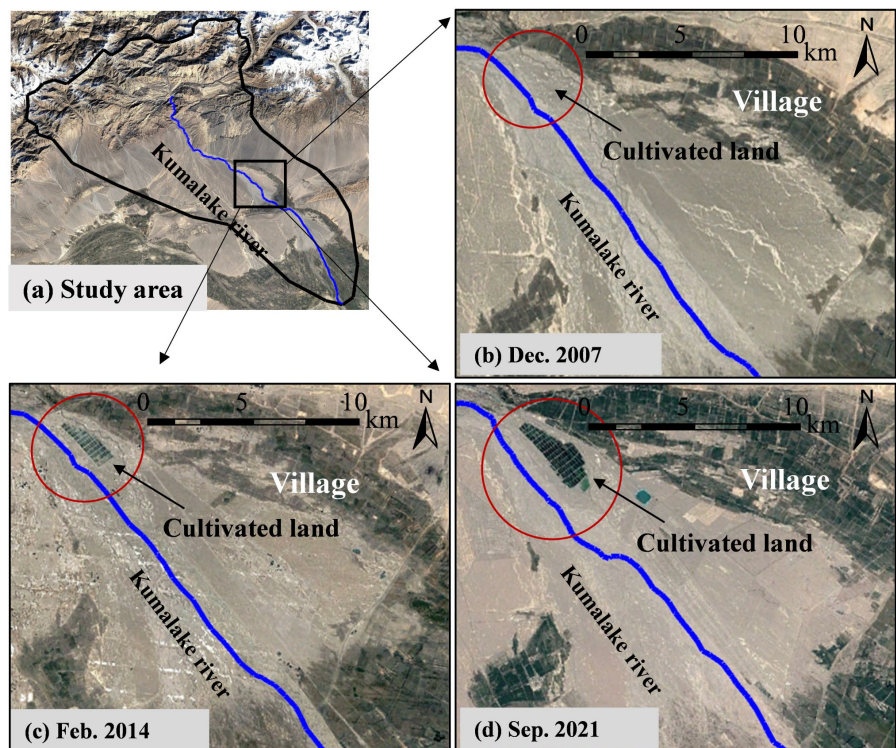


Figure 11. The predicted Kumalake River channel at December 2021.

Remote sensing images (Fig. 12) collected during the simulation period of the study area indicates that, beginning in 2012, the villages along the river initiated to develop cultivated land near the river channel. This anthropogenic activity altered key parameters related to land cover and soil type, and may have been a driving factor for the gradual southward migration of local river reaches. However, this mechanism of human-induced change is not explicitly represented in the landscape evolution model, which may partly explain the reduced simulation accuracy in the downstream region. Nevertheless, the parameter uncertainty analysis conducted in this study helps to partially compensate for the effects of land reclamation, keeping the prediction deviation of basin-scale river channel migration model within an acceptable range.



448
449 **Figure 12.** Formation process of cultivated land along the river in the study area. Satellite
450 imagery: © Google Earth 2007, 2014, 2021, modified by the authors.

451 **4.2 Prediction of river channel migration in future (2021-2100)**

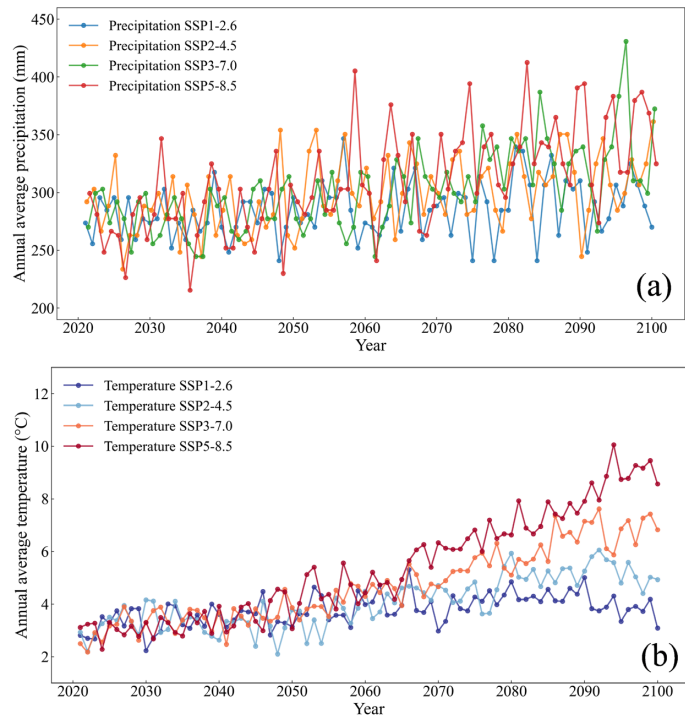
452 Future climate change will influence landscape evolution and river channel migration,
453 thereby affecting regional water resource patterns and ecological environments. The EC-
454 Earth3-Veg climate model, released under phase 6 of the Coupled Model Intercomparison
455 Project (CMIP6), incorporates vegetation-climate interactions and is well-suited for
456 evaluating terrestrial ecosystem and hydrological responses under different climate
457 scenarios (Alsalal et al., 2024; Eyring et al., 2016). Based on the EC-Earth3-Veg model,
458 this study adopts four scenarios of shared socioeconomic pathways (SSPs), i.e., SSP1-2.6,
459 SSP2-4.5, SSP3-7.0, and SSP5-8.5. Each of the four climate scenarios reflects a distinct



460 pathway of global socioeconomic development and associated impacts on greenhouse gas
461 emissions and climate change (O'Neill et al., 2016). Scenario-based simulations of
462 landscape evolution and river channel migration were conducted by using these climate
463 conditions as the driving force of LE-PIHM. The climate conditions for these scenarios
464 over the simulation period (2021–2100) are characterized by the annual mean temperature
465 and precipitation (Table 5 and Fig. 13).

466 **Table 5.** Statistics of four climate scenarios under the EC-Earth3-Veg model.

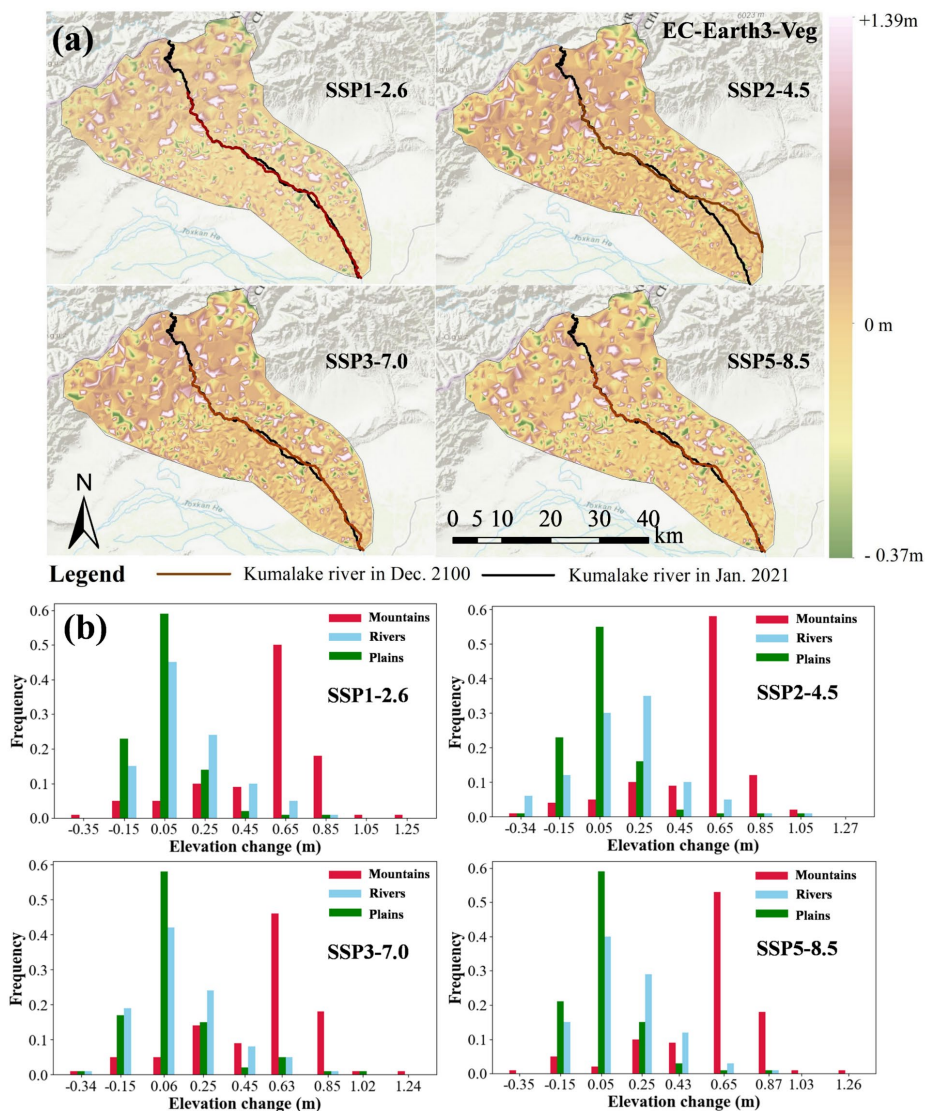
Climate model	Average precipitation	Average temperature	Shared Socioeconomic Pathways
EC-Earth3-Veg	284.97mm	3.76°C	SSP-1.26
	300.89mm	4.05°C	SSP-2.45
	301.76mm	4.68°C	SSP-3.70
	310.16mm	5.33°C	SSP-5.85



467
468 **Figure 13.** Annual mean precipitation and temperature for the four climate scenarios.



469 Using LE-PIHM and the parameter set corresponding to the maximum likelihood
470 estimate (Table 4), the landscape evolution and river channel migration from 2021 to 2100
471 were simulated for the study area under four climate change scenarios. After 80 years of
472 simulated landscape evolution, the overall topographic pattern of the region remains
473 characterized by higher elevations in the north and lower elevations in the south, with
474 elevation changes ranging from +1.39 m to -0.37 m. The simulation results under the four
475 EC-Earth3-Veg climate scenarios demonstrate that the elevation change and river channel
476 migration in basin scale by the year 2100 exhibit distinct characteristics (Fig. 14 a). In the
477 northern mountainous area, distinct alternating patterns of uplift and subsidence are
478 observed, with relatively large magnitudes of change. This is primarily due to intense
479 bedrock weathering and steep slopes in the mountains, where the regolith layer is thin and
480 the weathered soil and sediment are prone to downslope transport into adjacent low-lying
481 regions, resulting in significant elevation fluctuations. In contrast, the southern plain
482 exhibits gentle topography and minimal elevation differences, making it less conducive to
483 large-scale sediment transport. As a result, the landscape undulation in the plain is
484 relatively mild and limited in amplitude.



485

486 **Figure 14.** Spatial distribution of river channel (a) and Elevation change (b) under four
487 future climate scenarios based on the EC-Earth3-Veg climate model. Basemap: Esri
488 World Hillshade (Esri).

489 Under the EC-Earth3-Veg climate model, the four future climate scenarios induce
490 distinct patterns of river channel migration. By the end of the simulation period (2100), the
491 upstream reaches of the Kumalake River remain largely unchanged from their 2021



492 positions. This stability is attributed to the fact that these reaches flow through narrow and
493 geomorphologically stable canyon landscape, where external disturbances are minimal and
494 the river alignment and morphology remain relatively constant. In contrast, several
495 downstream reaches situated in the plain exhibit varying degrees of northward migration.
496 This phenomenon is mainly driven by the relatively gentle topography of the plains,
497 increased sediment deposition, redistribution of flow energy, and anthropogenic activities.
498 These factors collectively lead to channel swinging, incision, or aggradation, gradually
499 shifting the river channel position.

500 The four scenarios under EC-Earth3-Veg exhibit significant differences in
501 temperature and precipitation characteristics, as well as in the extent of river channel
502 migration (Table 6). Notably, under the SSP2-4.5 scenario, although the climate variability
503 is not the most intense among the scenarios, the elevation change shows the largest
504 amplitude, and the topographic changes in the river area are more pronounced (Fig. 14 b),
505 leading to a shift of the downstream river channels into the plain area. The specific
506 combination of climatic conditions may cause the river system to approach an evolutionary
507 threshold (Church et al., 2002; Meyer et al., 2018). When such a critical threshold is
508 reached, the river system may undergo abrupt transitions, manifesting as regime shifts
509 (Church et al., 2002). Under this scenario (SSP2-4.5), the downstream river channel
510 deviates entirely from its initial position, with an average Hausdorff distance reaching
511 1,873.37 m, primarily in the northward direction. This suggests that the climate changes in
512 this scenario trigger a sudden and intense spatial reorganization of the river network,
513 resulting in significant morphological transformation.

514 These results indicate that the process of river channel migration in the study area



515 under climate forcing varies across scenarios. Future climate conditions play a critical role
516 in regional landscape evolution and river dynamics. Furthermore, the complex feedbacks
517 between climate change and geomorphic systems highlight the importance of incorporating
518 these interactions in predictive modeling of fluvial landscape evolution and watershed
519 management planning.

520 **Table 6.** Statistics of climate scenarios and average Hausdorff distance of river migration.

	SSP1-2.6	SSP2-4.5	SSP3-7.0	SSP5-8.5
Variance of precipitation (mm ²)	576	922.45	1227.62	1942.72
Range of precipitation (mm)	105.85	127.75	186.15	197.1
Variance of temperature (°C ²)	0.34	0.92	1.99	4.27
Range of temperature (°C)	3.08	3.96	5.45	7.79
H(m)	333.26	1873.37	405.69	304.85

521 **5. Conclusions**

522 River channel migration at the basin scale not only determines the spatial distribution
523 pattern of regional river networks, but also exerts profound influences on local ecosystems
524 and the development of civilizations within the basin. Simulating river channel migration
525 at the basin scale aids in quantitatively reconstructing this long-term, complex dynamic
526 processes and also provides a scientific basis for decision-making in response to climate
527 change and natural disasters. To address the limitations of traditional river channel
528 migration models in temporal and spatial scale applications, this study integrates a
529 landscape evolution model with river channel extraction techniques, achieving accurate
530 and reliable simulation of river channel migration processes at the basin scale. Using the
531 Kumalake River Basin as a case study, the river channel migration process in the region is
532 reconstructed based on the LE-PIHM landscape evolution model and river channel
533 extraction techniques. The main conclusions of this study are as follows:



534 1. The LSTM-based surrogate model for river channel migration demonstrates high
535 accuracy and effectively overcomes the computational challenge associated with parameter
536 uncertainty analysis. The parameter calibration using MCMC requires numerous
537 executions of the LE-PIHM model and river channel extraction, resulting in prohibitive
538 computational demands. The surrogate model for basin-scale river channel migration based
539 on LSTM networks accurately characterizes the response relationship between landscape
540 evolution parameters and river channel locations, effectively solving the problem of
541 computational burden in Bayesian uncertainty analysis.

542 2. The river channel migration model facilitated by Bayesian parameter uncertainty
543 quantification can reliably predict the river channel evolution process within the study area.
544 Based on the inferred posterior distributions of model parameters, the predicted confidence
545 interval of the channel fully encompasses the actual river location. The average Hausdorff
546 distance between the simulated river channel with the maximum likelihood parameter set
547 and the observed river channel is 225.42 m, which accounts for only 0.25% of the total
548 channel length. Thus, the basin-scale river channel migration model incorporating
549 Bayesian uncertainty analysis demonstrates high reliability and predictive capability,
550 enabling effective characterization of river migration processes within the study area.

551 3. River channel evolution under different climate scenarios demonstrates significant
552 variability, and future climate change will profoundly affect basin geomorphological
553 characteristics and river network configurations. Based on the EC-Earth3-Veg model
554 released by CMIP6, the landscape evolution and river channel migration in the study area
555 from 2021 to 2100 were projected under four Shared Socioeconomic Pathways (SSP1-2.6,



556 SSP2-4.5, SSP3-7.0, and SSP5-8.5). The results indicate that climate change and
557 geomorphological systems exhibit complex response mechanisms.

558 ***Author contributions.***

559 JW and XZ conceptualized the study and designed the research methodology. JW and
560 QW conducted the simulations and implemented the methodology. JW produced all the
561 figures and tables. XZ and JW contributed to the data validation and data curation. DW
562 supervised the research. All authors reviewed, edited and approved the final version of the
563 manuscript.

564 ***Competing interest.***

565 The contact author has declared that none of the authors has any competing interests.

566 ***Data Availability.***

567 The temperature and precipitation data used in this study from the World Data Center
568 for Climate (WDCC) are open-access and publicly available: EC-Earth-Consortium EC-
569 Earth3-Veg (<https://doi.org/10.26050/WDCC/AR6.C6CMEEVE>, CMIP6). The observed
570 river channel planform data used for uncertainty analysis mentioned in Sect. 3.3 have been
571 made publicly available via the Hydroshare platform
572 (<https://doi.org/10.4211/hs.a6eb2a2c8ae746cf99d5d89a5ed2600b>, Zeng and Wu., 2025).

573 ***Acknowledgments.***

574 This study was supported by the National Key Research and Development Program
575 of China (2024YFC3713001), the National Natural Science Foundation of China
576 (42477082). We are grateful to the High-Performance Computing Center (HPCC) of
577 Nanjing University for performing the simulations in this paper.

578

579



580 **References**

- 581 Ali, M. S., Hasan, M. M., and Haque, M.: Two-dimensional simulation of flows in an open
 582 channel with groin-like structures by iRIC Nays2DH, *Math. Probl. Eng.*, 2017,
 583 1275498, <https://doi.org/10.1155/2017/1275498>, 2017.
- 584 Alsallal, S., Tan, M. L., Samat, N., Al-Bakri, J. T., and Zhang, F.: Temperature and
 585 precipitation changes under CMIP6 projections in the Mujib Basin, Jordan, *Theor.*
 586 *Appl. Climatol.*, 155, 7703–7720, <https://doi.org/10.1007/s00704-024-05087-2>, 2024.
- 587 Barnhart, K. R., Hutton, E. W. H., Tucker, G. E., Gasparini, N. M., Istanbuluoglu, E.,
 588 Hobley, D. E. J., Lyons, N. J., Mouchene, M., Nudurupati, S. S., Adams, J. M., and
 589 Bandaragoda, C.: Short communication: Landlab v2.0: a software package for Earth
 590 surface dynamics, *Earth Surf. Dynam.*, 8, 379–397, [https://doi.org/10.5194/esurf-8-](https://doi.org/10.5194/esurf-8-379-2020)
 591 379-2020, 2020.
- 592 Bishop, P.: Long-term landscape evolution: linking tectonics and surface processes, *Earth*
 593 *Surf. Process. Landf.*, 32, 329–365, <https://doi.org/10.1002/esp.1493>, 2007.
- 594 Braun, J. and Sambridge, M.: Modeling landscape evolution on geological time scales: a
 595 new method based on irregular spatial discretization, *Basin Res.*, 9, 27–52,
 596 <https://doi.org/10.1046/j.1365-2117.1997.00030.x>, 1997.
- 597 Church, M.: Geomorphic thresholds in riverine landscapes, *Freshw. Biol.*, 47, 541–557,
 598 <https://doi.org/10.1046/j.1365-2427.2002.00919.x>, 2002.
- 599 Coulthard, T. J., Neal, J. C., Bates, P. D., Ramirez, J., de Almeida, G. A., and Hancock, G.
 600 R.: Integrating the LISFLOOD-FP 2D hydrodynamic model with the CAESAR model:
 601 implications for modelling landscape evolution, *Earth Surf. Process. Landf.*, 38,
 602 1897–1906, <https://doi.org/10.1002/esp.3478>, 2013.
- 603 Desormeaux, C., Godard, V., Lague, D., Duclaux, G., Fleury, J., Benedetti, L., Bellier, O.,
 604 and the ASTER Team: Investigation of stochastic-threshold incision models across a
 605 climatic and morphological gradient, *Earth Surf. Dynam.*, 10, 473–492,
 606 <https://doi.org/10.5194/esurf-10-473-2022>, 2022.



- 607 ESRI: ArcGIS Pro, Esri, available at: [https://www.esri.com/en-](https://www.esri.com/en-us/legal/requirements/open-source-acknowledgements)
 608 [us/legal/requirements/open-source-acknowledgements](https://www.esri.com/en-us/legal/requirements/open-source-acknowledgements), last access: 6 December 2023,
 609 2022.
- 610 Eyring, V., Bony, S., Meehl, G. A., Senior, C. A., Stevens, B., Stouffer, R. J., and Taylor,
 611 K. E.: Overview of the Coupled Model Intercomparison Project Phase 6 (CMIP6)
 612 experimental design and organization, *Geosci. Model Dev.*, 9, 1937–1958,
 613 <https://doi.org/10.5194/gmd-9-1937-2016>, 2016.
- 614 Goren, L., Willett, S. D., Herman, F., and Braun, J.: Coupled numerical–analytical
 615 approach to landscape evolution modeling, *Earth Surf. Process. Landf.*, 39, 522–545,
 616 <https://doi.org/10.1002/esp.3514>, 2014.
- 617 Graves, A. and Schmidhuber, J.: Framewise phoneme classification with bidirectional
 618 LSTM and other neural network architectures, *Neural Netw.*, 18, 602–610,
 619 <https://doi.org/10.1016/j.neunet.2005.06.042>, 2005.
- 620 Hickin, E. J.: River channel changes: retrospect and prospect, in: *Modern and ancient*
 621 *fluvial systems*, 59–83, <https://doi.org/10.1002/9781444303773.ch5>, 1983.
- 622 Hochreiter, S. and Schmidhuber, J.: Long short-term memory, *Neural Comput.*, 9, 1735–
 623 1780, <https://doi.org/10.1162/neco.1997.9.8.1735>, 1997.
- 624 Hou, R., Zeng, X., Wang, D., and Wu, J.: Evaluating spatial downscaling surrogate models
 625 for landscape evolution simulations in the Tarim River basin, China, *Stoch. Environ.*
 626 *Res. Risk Assess.*, 39, 2479–2496, <https://doi.org/10.1007/s00477-025-02980-8>,
 627 2025.
- 628 Hritz, C.: Tracing settlement patterns and channel systems in southern Mesopotamia using
 629 remote sensing, *J. Field Archaeol.*, 35, 184–203,
 630 <https://doi.org/10.1179/009346910X12707321520477>, 2010.
- 631 Hsu, S. Y. and Hsu, S. M.: Morphological evolution mechanism of gravel-bed braided river
 632 by numerical simulation on Da-Jia River, *J. Hydrol.*, 613, 128222,
 633 <https://doi.org/10.1016/j.jhydrol.2022.128222>, 2022.



- 634 Ikeda, S., Parker, G., and Sawai, K.: Bend theory of river meanders, Part 1: Linear
 635 development, *J. Fluid Mech.*, 112, 363–377,
 636 <https://doi.org/10.1017/S0022112081000451>, 1981.
- 637 Lesser, G., Roelvink, D., van Kester, J., and Stelling, G.: Development and application of
 638 a three-dimensional model for coastal morphology and hydrodynamics, *Coast. Eng.*,
 639 51, 883–915, <https://doi.org/10.1016/j.coastaleng.2004.07.014>, 2004.
- 640 Li, K., Qin, X., Xu, B., Yin, Z., Wu, Y., Mu, G., Wei, D., Tian, X., Shao, H., Wang, C.,
 641 Jia, H., Li, W., Song, H., Liu, J., and Jiao, Y.: Hydro-climatic aspects of prehistoric
 642 human dynamics in the drylands of the Asian interior, *Holocene*, 33, 194–207,
 643 <https://doi.org/10.1177/09596836221131694>, 2023.
- 644 Lisenby, P. E., Fryirs, K. A., and Thompson, C. J.: River sensitivity and sediment
 645 connectivity as tools for assessing future geomorphic channel behavior, *Int. J. River*
 646 *Basin Manag.*, 18, 279–293, <https://doi.org/10.1080/15715124.2019.1672705>, 2020.
- 647 Litwin, D. G., Tucker, G. E., Barnhart, K. R., and Harman, C. J.: Catchment coevolution
 648 and the geomorphic origins of variable source area hydrology, *Water Resour. Res.*,
 649 60, e2023WR034647, <https://doi.org/10.1029/2023WR034647>, 2024.
- 650 Meyer, K., Hoyer-Leitzel, A., Iams, S., Klasky, I., Lee, V., Ligtenberg, S., Bussmann, E.,
 651 and Zeeman, M. L.: Quantifying resilience to recurrent ecosystem disturbances using
 652 flow-kick dynamics, *Nat. Sustain.*, 1, 671–678, [https://doi.org/10.1038/s41893-018-](https://doi.org/10.1038/s41893-018-0168-z)
 653 [0168-z](https://doi.org/10.1038/s41893-018-0168-z), 2018.
- 654 Morón, S., Edmonds, D., and Amos, K.: The role of floodplain width and alluvial bar
 655 growth as a precursor for the formation of anabranching rivers, *Geomorphology*, 278,
 656 78–90, <https://doi.org/10.1016/j.geomorph.2016.10.026>, 2017.
- 657 Neuendorf, F., von Haaren, C., and Albert, C.: Assessing and coping with uncertainties in
 658 landscape planning: an overview, *Landscape Ecol.*, 33, 861–878,
 659 <https://doi.org/10.1007/s10980-018-0643-y>, 2018.
- 660 O’Callaghan, J. F. and Mark, D. M.: The extraction of drainage networks from digital
 661 elevation data, *Comput. Vis. Graph. Image Process.*, 28, 323–344,
 662 [https://doi.org/10.1016/S0734-189X\(84\)80011-0](https://doi.org/10.1016/S0734-189X(84)80011-0), 1984.



- 663 O'Neill, B. C., Tebaldi, C., van Vuuren, D. P., Eyring, V., Friedlingstein, P., Hurtt, G.,
 664 Knutti, R., Kriegler, E., Lamarque, J.-F., Lowe, J., Meehl, G. A., Moss, R., Riahi, K.,
 665 and Sanderson, B. M.: The Scenario Model Intercomparison Project (ScenarioMIP)
 666 for CMIP6, *Geosci. Model Dev.*, 9, 3461–3482, [https://doi.org/10.5194/gmd-9-3461-](https://doi.org/10.5194/gmd-9-3461-2016)
 667 2016, 2016.
- 668 Qu, Y. and Duffy, C. J.: A semidiscrete finite volume formulation for multiprocess
 669 watershed simulation, *Water Resour. Res.*, 43, W08419,
 670 <https://doi.org/10.1029/2006WR005752>, 2007.
- 671 Schütze, O., Esquivel, X., Lara, A., and Coello, C. A. C.: Using the averaged Hausdorff
 672 distance as a performance measure in evolutionary multiobjective optimization, *IEEE*
 673 *Trans. Evol. Comput.*, 16, 504–522, <https://doi.org/10.1109/TEVC.2011.2161872>,
 674 2012.
- 675 Shao, Y., Gong, H., Elachi, C., Brisco, B., Liu, J., Xia, X., Guo, H., Geng, Y., Kang, S.,
 676 Liu, C., Yang, Z., and Zhang, T.: The lake-level changes of Lop Nur over the past
 677 2000 years and its linkage to the decline of the ancient Loulan Kingdom, *J. Hydrol.*
 678 *Reg. Stud.*, 40, 101002, <https://doi.org/10.1016/j.ejrh.2022.101002>, 2022.
- 679 Tang, Q., Hu, H., Oki, T., and Tian, F.: Water balance within intensively cultivated alluvial
 680 plain in an arid environment, *Water Resour. Manag.*, 21, 1703–1715,
 681 <https://doi.org/10.1007/s11269-006-9121-4>, 2007.
- 682 Tarboton, D. G.: A new method for the determination of flow directions and upslope areas
 683 in grid digital elevation models, *Water Resour. Res.*, 33, 309–319,
 684 <https://doi.org/10.1029/96WR03137>, 1997.
- 685 Temme, A. J. A. M., Heuvelink, G. B. M., Schoorl, J. M., and Claessens, L.: Geostatistical
 686 simulation and error propagation in geomorphometry, in: *Geomorphometry: Concepts,*
 687 *Software, Applications*, edited by: Hengl, T. and Reuter, H. I., *Developments in Soil*
 688 *Science*, 33, 121–140, [https://doi.org/10.1016/S0166-2481\(08\)00005-6](https://doi.org/10.1016/S0166-2481(08)00005-6), 2009.
- 689 Tucker, G. E. and Hancock, G. R.: Modelling landscape evolution, *Earth Surf. Process.*
 690 *Landf.*, 35, 28–50, <https://doi.org/10.1002/esp.1952>, 2010.



- 691 Tucker, G., Lancaster, S., Gasparini, N., and Bras, R.: The channel-hillslope integrated
 692 landscape development model (CHILD), in: Landscape erosion and evolution
 693 modeling, edited by: Harmon, R. S. and Doe, W. W., 349–388,
 694 https://doi.org/10.1007/978-1-4615-0575-4_12, 2001.
- 695 Vrugt, J. A., ter Braak, C. J. F., Diks, C. G. H., Robinson, B. A., Hyman, J. M., and Higdon,
 696 D.: Accelerating Markov chain Monte Carlo simulation by differential evolution with
 697 self-adaptive randomized subspace sampling, *Int. J. Nonlinear Sci. Numer. Simul.*, 10,
 698 273–290, <https://doi.org/10.1515/IJNSNS.2009.10.3.273>, 2009.
- 699 Wang, M. and Shen, Z. K.: Present-day crustal deformation of continental China derived
 700 from GPS and its tectonic implications, *J. Geophys. Res. Solid Earth*, 125,
 701 e2019JB018774, <https://doi.org/10.1029/2019JB018774>, 2020.
- 702 Wang, Y., Zhou, Y., Wu, S., and Peng, X.: Colonize the desert vs. retreat to the mountains:
 703 The evolution of city–water relationships in the Tarim river basin over the past 2000
 704 years, *Appl. Geogr.*, 170, 103346, <https://doi.org/10.1016/j.apgeog.2024.103346>,
 705 2024.
- 706 Whipple, K. X., Forte, A. M., DiBiase, R. A., Gasparini, N. M., and Ouimet, W. B.:
 707 Timescales of landscape response to divide migration and drainage capture:
 708 Implications for the role of divide mobility in landscape evolution, *J. Geophys. Res.*
 709 *Earth Surf.*, 122, 248–273, <https://doi.org/10.1002/2016JF003973>, 2017.
- 710 Yang, R., Willett, S. D., and Goren, L.: In situ low-relief landscape formation as a result
 711 of river network disruption, *Nature*, 520, 526–529,
 712 <https://doi.org/10.1038/nature14354>, 2015.
- 713 Yu, G. A., Disse, M., Huang, H. Q., Yu, Y., and Li, Z.: River network evolution and fluvial
 714 process responses to human activity in a hyper-arid environment – case of the Tarim
 715 River in Northwest China, *Catena*, 147, 96–109,
 716 <https://doi.org/10.1016/j.catena.2016.06.038>, 2016.
- 717 Zhang, Y., Slingerland, R., and Duffy, C.: Fully-coupled hydrologic processes for
 718 modeling landscape evolution, *Environ. Model. Softw.*, 82, 89–107,
 719 <https://doi.org/10.1016/j.envsoft.2016.04.014>, 2016.



- 720 Zhen, J., Guo, Y., Wang, Y., Li, Y., and Shen, Y.: Spatial–temporal evolution and driving
721 factors of water–energy–food–ecology coordinated development in the Tarim River
722 Basin, *J. Hydrol. Reg. Stud.*, 58, 102288, <https://doi.org/10.1016/j.ejrh.2025.102288>,
723 2025.
- 724 Zhou, Y., Gao, Y., Shen, Q., Yan, X., Liu, X., Zhu, S., Lai, Y., Li, Z., and Lai, Z.: Response
725 of channel morphology to climate change over the past 2000 years using vertical
726 boreholes analysis in the Lancang River headwater in the Tibetan Plateau, *Water*, 14,
727 1593, <https://doi.org/10.3390/w14101593>, 2022.
- 728 Zeng, X. and Wu, J.: Numerical simulation of basin-scale river channel migration driven
729 by landscape evolution, *HydroShare* [data set],
730 <https://doi.org/10.4211/hs.a6eb2a2c8ae746cf99d5d89a5ed2600b>, 2025.
- 731 Zubovich, A., Schöne, T., Metzger, S., Mosienko, O., Mukhamediev, S., Sharshebaev, A.,
732 and Zech, C.: Tectonic interaction between the Pamir and Tien Shan observed by GPS,
733 *Tectonics*, 35, 283–292, <https://doi.org/10.1002/2015TC004055>, 2016.